Pergamon

Solid-State Electronics Vol. 42, No. 1, pp. 1–15, 1998

Printed in Great Britain

PII: S0038-1101(97)00238-4

0038-1101/98 $19.00 + 0.00

INVITED PAPER

LASER INFRARED PHOTOTHERMAL RADIOMETRY OF SEMICONDUCTORS: PRINCIPLES AND APPLICATIONS TO SOLID STATE ELECTRONICS

ANDREAS MANDELIS

Photothermal and Optoelectronic Diagnostics Laboratories, Department of Mechanical and Industrial Engineering, University of Toronto, Toronto, Canada M5S 3G8

(Received 23 May 1997)

Abstract—The photothermal origins and physical principles of the novel diagnostic technique of laser infrared photothermal radiometry of semiconductors are presented. Following super-bandgap optical excitation, it is shown that the signal consists of two contributions, one from the de-exciting carrier density (plasma wave) and another from direct absorption and heating of the lattice (thermal wave). The advantage of this technique over other photothermal methods in the field of diagnostics in solid-state electronics lies with the domination of the signal by the plasma wave component over a broad high-frequency range, quite accessible by today's electronic instrumentation. As a result, the primary photoinjected carrier parameters can be easily and reliably measured: lifetime, τ, electronic *and* thermal diffusivities, D and α, respectively, and surface recombination velocities, s_j, on both semiconductor wafer surfaces. The theoretical section is complemented with key applications chosen from a rapidly increasing set of case studies, including Si wafer substrate transport property diagnostics, contamination control of chemically cleaned process wafers, MOS capacitor structures, carrier lifetime depth profiles in ion-implanted wafers, and bulk crystalline and thin-film photoconductors. © 1998 Elsevier Science Ltd. All rights reserved

1. INTRODUCTION: PHOTOTHERMAL HEAT SOURCES IN ELECTRONIC MATERIALS

When a semiconductor is optically excited with monochromatic photons of energy $\hbar\omega_0$ greater than, or on the order of, the fundamental energy gap E_g, several dynamic processes may occur, which result in the generation of thermal energy sources in the semiconductor. Figure 1 is a schematic of various energetic de-excitation processes following laser radiation absorption. There exists a number of comprehensive books in the general case, such as those edited by Hess[1], Mandelis[2] and the monograph by Bialkowski[3]. For the purposes of the infrared radiometric methods presented in this paper, only the heat and radiation generation branches of the de-excitation manifold of a semiconductor will be discussed, starting with de-excitation processes immediately after the absorption of laser radiation:

(1). At the early times after the deposition of the optical energy, energetic electron–hole pairs are created possessing kinetic energies $(\hbar\omega - E_g)$. These carriers progressively suffer collisions with other carriers and lattice phonons, until thermal equilibrium is achieved. Some characteristic times involved in the intraband relaxation of carriers in Si and Ge following the absorption of ultrashort pulses of coherent electromagnetic radiation are shown in Table 1[4]. Assuming an average intraband relaxation time $\tau_{IB} \sim 10^{-12}$ s[5], effects due to intraband thermal diffusion may be neglected on the time scale of the conventional frequency domain photothermal response of the semiconductor and the heat source profile can be accurately described by the optical absorption distribution

$$H_{IB}(\mathbf{r}, t; \lambda) = \eta_G N_o(t)(\hbar\omega_0 - E_g) \times \exp[-\beta(\lambda)|r|] \ [\mathrm{W/cm^3}] \quad (1)$$

where H_{IB} $(\mathbf{r}, t; \lambda)$ is the intraband heat release rate per unit volume of the optically excited semiconductor, η_G is the quantum efficiency for photogenerated carriers, $\beta(\lambda)$ is the optical absorption coefficient at the excitation wavelength λ, and N_o is the photon deposition rate per unit volume.

(2) Photogenerated carriers will diffuse during their lifetime τ in the conduction (and/or valence) band through distances equal, on the average, to the respective diffusion length $L_c = (D_c\tau_c)^{1/2}$, where c = n (electron) or p (hole). Following diffusive spatial migration, excess electron–hole pairs generate a thermal wave source through non-radiative bulk interband recombinations[6]. The heat release rate per unit volume due to non-radiative recombination is given by Bandeira *et al.*[5]; Thielemann and Rheinländer,[7]

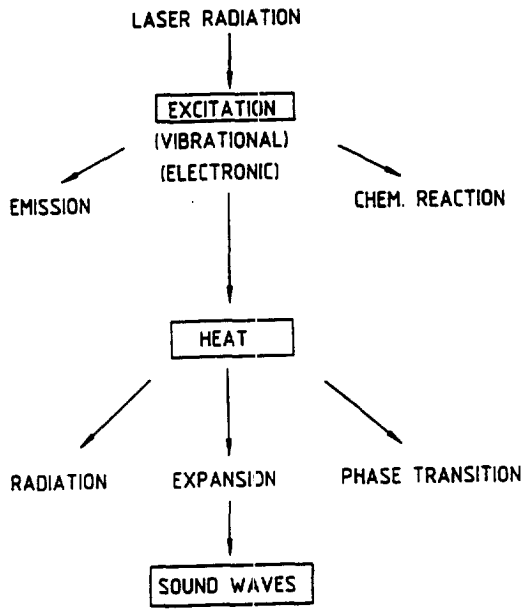

Fig. 1. General schematic of de-excitation processes in a solid following absorption of laser radiation

$$H_{BB}(r;\ t;\ \lambda) = \eta_G \eta_{NR} N_o(t) E_g \exp[-\beta(\lambda)|r|]\ [W/cm^3] \tag{2}$$

where η_{NR} is the non-radiative quantum efficiency. Equation (2) is only relevant when $\hbar\omega_o \geq E_g$.

(3) Front-surface (FS) and rear-surface (RS) non-radiative carrier recombination results in the generation of surface heat release rates per unit area given by Flaisher and Cahen[8]; Bandeira *et al.*[5]:

$$H_{FS}(0,\ t;\ \lambda) = \eta_{FS}[n(0,\ t;\ \lambda) - n_o] S_{FS} E_g\ [W/cm^2] \tag{3a}$$

and

$$H_{RS}(L,\ t;\ \lambda) = \eta_{RS}[n(L,\ t;\ \lambda) - n_o] S_{RS} E_g\ [W/cm^2] \tag{3b}$$

where η_{FS} (η_{RS}) is the front (rear) surface non-radiative quantum efficiency, $n(z,\ t;\ \lambda)$ is the photogenerated electron density distribution in a one-dimensional geometry, n_e is the equilibrium electron density, and S_{FS} (S_{RS}) is the front (rear) recombination velocity. Equations (3a)–(b) are valid for n-type semiconductors; a pair of similar equations can be written for p-type materials with $n \rightarrow p$, in Equations (3a)–(b). In an actual experimental situation the thermal source generated due to pulsed or harmonically modulated optical absorption in a semiconductor will be the superposition of all the foregoing heating rates.

Table 1. Important carrier and lattice characteristic times in Si and Ge[a]

Phenomenon	Characteristic time (s)
Carrier Coulomb thermalization	$< 10^{-14}$
Carrier momentum relaxation	10^{-13}
Carrier-LO-phonon thermalization	10^{-12}
LO-phonon–acoustic-phonon interaction	10^{-12}–10^{-11}
Auger recombination ($N = 10^{20}$ cm^{-3})	10^{-10}
Impact ionization ($N = 10^{20}$ cm^{-3}, $T_e = 10^3$ K)	$> 10^{-4}$
1-μm carrier diffusion time	10^{-10}
1-μm lattice heat diffusion time	10^{-8}

[a]After van Driel[4].

2. PHYSICAL FOUNDATIONS OF LASER INFRARED PHOTOTHERMAL RADIOMETRY OF SEMICONDUCTORS

Historically, infrared photothermal radiometry (PTR) was first applied by Nordal and Kanstad[9] to obtain, without contact, optical absorption spectra of non-electronic materials. When an absorbing solid is irradiated by intensity-modulated light, the modulation of the surface temperature rise, resulting from radiation absorption and non-radiative energy conversion, can be monitored through the oscillation of the infrared (IR) blackbody (Planck) emission from the surface and the bulk. By measuring such variations in the IR radiant emittance, Nordal and Kanstad were able to obtain information about a sample's spectral and/or thermophysical properties. This method is sensitive to the surface temperature of a solid only, and not, to its bulk temperature, provided that the solid is opaque to the incident radiation *and* to the IR wavelength range used for detection. The physical basis for PTR detection is the blackbody radiation law, which describes the total radiant emittance, W, over infinite detection bandwidth, of a body at thermal equilibrium at temperature T:

$$W = \epsilon\sigma T^4\ [W/cm^2] \tag{4}$$

where σ is the Stefan–Boltzmann constant ($= 5.67 \times 10^{-12}$ W/cm^2 K^4) and ϵ is the emissivity. If the photothermally induced change in the surface temperature, $\Delta T(\omega)$, is small compared to the equilibrium temperature, the change in the radiant emittance is

$$\Delta W(\omega) \approx 4\epsilon\sigma T^3 \Delta T(\omega) \tag{5}$$

In recent years, extensive development of PTR has led to novel non-destructive evaluation methodologies for materials research[10], and for biomedical diagnostics[11,12]. In the first PTR application to electronic solids, Nakamura *et al.*[13] observed microdefects in GaAs with a PTR microscope. They measured the signal as a function of excitation energy at a low modulation frequency (330 Hz), thus obtaining a PTR spectrum. The same group also constructed the spatial distribution of PTR intensity (PTR imaging) of various GaAs wafers at room temperature and at the excitation wavelength of 895 nm[14]. They compared their images with dislocation density profiles and concluded that the PTR signal originated at non-radiative defects gen-

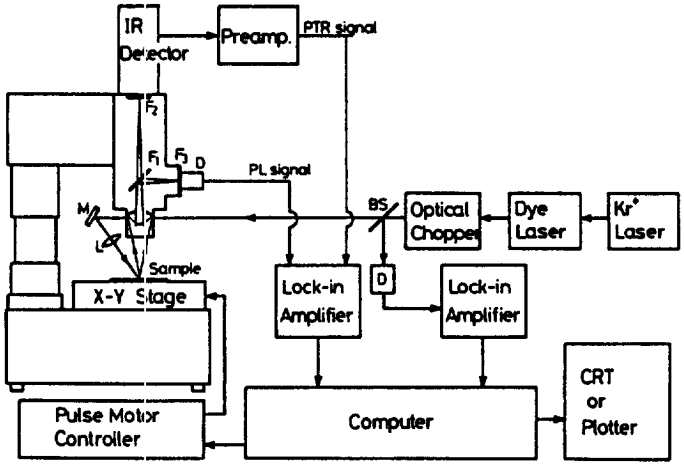

Fig. 2. Schematic diagram of the PTR microscope used for spectroscopic and imaging diagnostics of semiconductors (From Ref.[13].)

erated predominantly in the low-dislocation-density regions of the wafer. The PTR microscope utilized by Nakamura *et al.*[13] is shown in Fig. 2. Frequency-scanned PTR signal amplitudes were subsequently used for application to the analysis of electronic materials[15] as an alternative to purely optical infrared techniques, which have been used for sometime to probe electron–hole plasma effects[16,17], carrier homogeneity[46], and ion-implantation parameters, including damage[18,19]. Ulmer and Frankl[20] had demonstrated that optically generated carriers increase the infrared (blackbody) emission from the surface of an electronic solid. Based on that work, Sheard *et al.*[21] and Little *et al.*[22] reported laser-beam-modulation-frequency-scanned PTR amplitude signals from silicon samples, and showed that they carry information on the recombination and diffusion of the free-carrier plasma. According to a statement of Kirchhoff's Law of Detailed Balance reflecting conservation of energy, *at thermodynamic equilibrium the rate of emission of blackbody radiation from the surface and throughout the bulk of a material can be measured from, and is exactly equal to, the rate of absorption of the radiation incident on the material per wavelength interval.* Therefore, the infrared emission spectrum for a de-excitation process in a semiconductor can be obtained directly from its (usually better known) absorption spectrum. Although the foregoing statement is strictly valid under conditions of thermodynamic equilibrium, in practice it has been found to have broader validity[23], and applicability to several non-equilibrium processes in semiconductors[20,24]. In PTR detection, it is rather the reverse application of Kirchhoff's Law of Detailed Balance that is exploited: As described in Section 1, optical absorption of a laser beam in the ultraviolet, visible or near-infrared (super-bandgap) spectral ranges in Si results in electronic excitation, primary ultrafast energy transfer and intraband thermalization processes in the excited state (carrier–carrier, carrier–lattice, carrier–defect/impurity collisions), followed by much slower ($\sim\mu$s range) interband recombination kinetics (band-to-band, band-to-defect, *etc.*). It is precisely this latter mechanism that PTR probes at the present stage in its instrumental evolution: following super-bandgap optical absorption and carrier excitation, the blackbody IR photon flux emission from the surface and from the bulk of a semiconductor is the result of both lattice absorption and thermalization, as well as elementary carrier de-excitation and blackbody radiation energy emission via recombination, integrated over the emission depth of the electronic solid. *The emission is equivalent to surface and bulk absorption of the same infrared photon flux integrated along the same coordinate*, in agreement with Kirchhoff's Law. Therefore, by virtue of this equivalence, which is further assumed to be valid under dynamic recombination conditions, the interception of carrier-recombination-generated, back-propagating blackbody emission radiation power arriving at the surface of a semiconductor yields information entirely equivalent to absorption of forward-propagating infrared radiation power resulting in carrier generation (band-to-band, defect-to-band *etc.*) and may be used to study these processes. The excess energy due to ultrafast carrier thermalization or direct lattice absorption and the subsequent rise of the lattice temperature is also detected as an additional increase in blackbody emission, in agreement with the blackbody radiation law, Equation (4). Given that the generation of this thermal energy is usually instantaneous on the time scale of the carrier recombination lifetime, this radiation source is, in principle, always superposed on the photocarrier (plasma) relaxation–emission source, but with a

generally different time constant governed by conduction heat transfer in the lattice and into the ambient. The evolution of the superposition radiation emitted by a semiconductor and collected within a fixed solid angle in the surrounding medium is focused on, and monitored by, an appropriate PTR detector.

The main advantage of PTR detection of electronic phenomena over conventional *static* optical techniques is that PTR is not limited by the opacity of a semiconductor to sub-bandgap radiation. PTR as a dynamic technique is a zero-baseline experimental method, whereas static optical techniques measure *changes* in optical properties of semiconductors. This amounts to a higher dynamic range of the PTR signals. The PTR advantage over *modulated* optical techniques lies in its ability to measure transport parameters *directly* related to the electronic quality of the material, such as lifetime, diffusion coefficient and surface recombination velocity: it monitors the photoexcited carrier density distribution via the dependence of the infrared emissive properties of the sample on it, and not the more complex optical interactions in the solid. The PTR advantage over other *modulated photothermal* techniques[25], lies in its higher sensitivity to carrier plasma-wave transport processes as discussed above, with clear domination of the signal by these (rather than thermal-wave) processes in the case of high-quality electronic materials. This is due to the fact that free carrier emission, at least in Si, prevails over thermal emission of infrared radiation[26].

3. THEORY OF PTR SIGNAL GENERATION AND DETECTION FROM ELECTRONIC SOLIDS

The configuration of a one-dimensional (1D) mathematical model used in PTR, adequate for monitoring of substrate wafers and thin-film devices, is shown in Fig. 3. The thickness of a semiconductor sample is assumed to be L. The solid is irradiated with a harmonically modulated laser beam of spatially homogeneous intensity. The photon energy $h\nu$ of the laser beam is assumed to be greater than the semiconductor bandgap, E_g, and the excess photoinjected minority density is small compared to the majority carrier density (low-injection limit). The photoexcited excess carrier density, $\Delta n(z, t)$, is given by solving the carrier continuity eqn[27]. For single modulation-frequency harmonic excitation, the continuity equation yields the plasma-wave density in terms of the temporal Fourier transform component, $\Delta N(z, \omega)$, of $\Delta n(z, t)$:

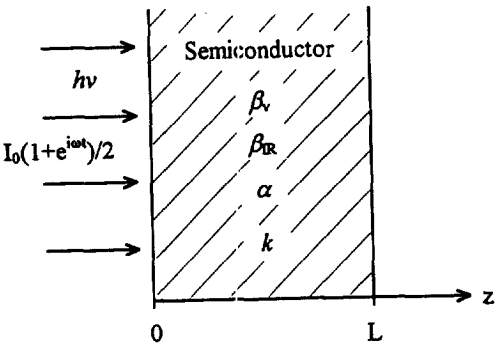

Fig. 3. Schematic of a one-dimensional geometry for the PTR signal theory, involving a modulated optical waveform of energy $h\nu > E_g$, intensity I_0, modulation angular frequency ω, and a semiconductor wafer of thickness L

$$D\frac{d^2\Delta N(z,\omega)}{dz^2} - \frac{\Delta N(z,\omega)}{\tau} + G(z,\omega) = i\omega\Delta N(z,\omega) \tag{6}$$

Here D (m^2/s) is the ambipolar diffusion coefficient, τ (s) is the carrier bulk lifetime, and $G(z, \omega)$ ($m^{-3}\,s^{-1}$) is the carrier generation rate. For harmonic laser-intensity modulation G is given by

$$G(z,\omega) = \frac{\beta\eta_G I_0 e^{-\beta z}}{2h\nu}(1 + e^{i\omega t}). \tag{7}$$

ω is the angular modulation frequency of the laser intensity I_0 (W/m^2), which illuminates the sample surface and is absorbed uniformly throughout its bulk with a (visible range) absorption coefficient $\beta_{vis} \equiv \beta$ (m^{-1}) and quantum efficiency η_G. The dc component of the solution of Equation (6) with the driving force term Equation (7) is ignored, since experimentally one uses synchronous lock-in detection which suppresses the dc background. Regarding the ac component, the most usual boundary conditions are

$$D\frac{d\Delta N(0,\omega)}{dz} = s_1\Delta N(0,\omega); \tag{8a}$$

and

$$D\frac{d\Delta N(L,\omega)}{dz} = -s_2\Delta N(L,\omega). \tag{8b}$$

Here s_j is the carrier surface recombination velocity (m/s) at $z = 0$ ($j = 1$) and $z = L$ ($j = 2$).

The boundary value problem of Equations (6)–(8a) and (8b) has been solved[15,28] to yield the free photoexcited carrier-wave dependence on the depth coordinate z and on modulation frequency. For laser excitation of an n-type material

$$\Delta N(z,\omega) = \frac{\beta\eta_G I_0}{2h\nu D_n(\beta^2 - \sigma_n^2)} \left(\frac{\gamma_1\Gamma_2 - \gamma_2\Gamma_1 e^{-(\beta+\sigma_n)L}}{\Gamma_2 - \Gamma_1 e^{-2\sigma_n L}} e^{-\sigma_n z} + \frac{\gamma_1 - \gamma_2 e^{-(\beta-\sigma_n)L}}{\Gamma_2 - \Gamma_1 e^{-2\sigma_n L}} e^{-\sigma_n(2L-z)} - e^{-\beta z} \right) \tag{9}$$

where the following definitions were made:

$$\Gamma_1 = \frac{D_n\sigma_n - s_1}{D_n\sigma_n + s_1}; \quad \Gamma_2 = \frac{D_n\sigma_n + s_2}{D_n\sigma_n - s_2} \tag{10}$$

and

$$\gamma_1 = \frac{D_n\beta + s_1}{D_n\sigma_n + s_1}; \quad \gamma_2 = \frac{D_n\beta - s_2}{D_n\sigma_n - s_2} \tag{11}$$

σ_n is the complex electron-carrier plasma diffusion wavenumber and is defined as

$$\sigma_n(\omega) \equiv \sqrt{(1 + i\omega\tau)/D_n\tau}\ [\mathrm{m}^{-1}] \tag{12}$$

For harmonically modulated optical excitation with super-bandgap radiation, the IR absorption coefficient, β_{IR}, is a function of the photo-excited free-carrier density in the semiconductor. Based on the free-plasma (Drude) model of the interaction of IR radiation with the semiconductor, Moss *et al.*[29] deduced a linear dependence of the β_{IR} on the free-carrier density N. Cho and Davis[24] showed experimentally that the simple linear dependence of β_{IR} on the carrier density is valid in the case of pulsed laser excitation of Si. A linear relationship was also shown to exist experimentally between the rate-window generated PTR signal and the photo-injected carrier density[30]. For harmonically modulated laser excitation, Mandelis *et al.*[31] also assumed a linear dependence of the form

$$\beta_{IR}(z;\ \omega,\ \lambda) = \beta^{o}_{IR}(z,\ \lambda) + \Delta\beta(z,\ \lambda)e^{i\omega t} \tag{13}$$

where the right-hand-side terms stand for the IR absorption coefficient in the dark (no illumination) and due to the photo-excited free carriers at modulation frequency $f = \omega/2\pi$, respectively. From the Drude model of Moss *et al.*[29], one obtains

$$\Delta\beta(z,\ \lambda;\ \lambda_{vis};\ \omega) = \frac{\lambda^2 q^3}{4\pi^2 c^3 n\epsilon_0 m^{*2}\mu}\Delta N(z;\ \lambda_{vis};\ \omega) \tag{14}$$

where q is the elementary charge; m^* is the effective mass of the photo-excited carriers; n is the infrared refractive index of the semiconductor; ϵ_0 is the permittivity of free space; and μ is the mobility of the photoexcited carriers. λ indicates the IR emission wavelength and λ_{vis} indicates the super-bandgap excitation wavelength. The temperature rise in the semiconductor due to lattice absorption, intraband de-excitation, and hot-electron interband recombination (Section 1) is

$$\Theta(z,\ \omega) = \Theta_0 + \Delta\Theta(z,\ \omega;\ \beta_{vis})e^{i\omega t} \tag{15}$$

Assuming a depth-independent IR absorption coefficient of a semiconductor, $\beta_{IR}(\lambda)$, the linear PTR signal in the one-dimensional model of the boundary value problem Equations (6)–(8a) and (8b) is given by Salnick *et al.*[26]:

$$S_{PTR}(\omega, \beta_{vis}) = C_T(\lambda_{vis}, \Theta_0, \lambda_1, \lambda_2)\int_0^L \Delta\Theta(z;\ \omega,\ \beta_{vis})\,dz + C_N(\lambda_{vis}, \Theta_0, \lambda_1, \lambda_2)\int_0^L \Delta N(z;\ \omega, \beta_{vis})\,dz\ [\mathrm{W}] \tag{16}$$

where the coefficients C_T and C_N are independent of the modulation frequency $f = \omega/2\pi$, but they depend on the ambient temperature Θ_0, and on the spectral range of the infrared detector $[\lambda_1, \lambda_2]$. C_T [W/mK] can be calculated using a Taylor expansion of Planck's distribution function to first order only, about the equilibrium (background) Θ_0 value for small perturbations, $\Delta\Theta(z;\ \omega,\ \beta_{vis})$, of the sample temperature[31]. It is given by

$$C_T = [1 - R(\lambda_{vis})]\int_{\lambda_1}^{\lambda_2}[1 - R(\lambda)]W_P(\lambda,\ \Theta_0) \times \left(\frac{hc\beta_{IR}(\lambda)}{\lambda k_B\Theta_0^2[\exp(hc/\lambda k_B\Theta_0) - 1]}\right)d\lambda\ [\mathrm{W/mK}] \tag{17}$$

where $R(\lambda)$ is the IR reflectivity of the semiconductor; $R(\lambda_{vis})$ is the reflectivity at the visible excitation wavelength; k_B is Boltzmann's constant; c is the speed of light in vacuum; and W_P is Planck's distribution function:

$$W_P(\lambda,\ \Theta_0) = \frac{2\pi hc^2 A}{\lambda^5[\exp(hc/\lambda k_B\Theta_0) - 1]},\ [\mathrm{W/m}] \tag{18}$$

where A is the emitting area of the sample surface. Using the classical model of wave propagation in a free plasma[29,32,33] with one type of dominant carrier density (n-type), and taking into account Equations (13)–(15), C_N [Wm^2] can be shown to be[34]

$$C_N = [1 - R(\lambda_{vis})]\int_{\lambda_1}^{\lambda_2}[1 - R(\lambda)]W_P(\lambda,\ \Theta_0) \times \frac{\lambda^2 q^3\,d\lambda}{4\pi^2 c^3\epsilon_0 n m_n^{*2}\mu_n}\ [\mathrm{Wm}^2] \tag{19}$$

In Equation (16), the functional dependencies of the integrands depend on the particulars of the plasma- and thermal-wave fields and can be calculated for specific experimental situations and geometries. For the carrier plasma-wave component, Equations (9)–(11) can be used. For the thermal-wave component, a number of simple one-dimensional models have been presented (see Mandelis[25]; Chap. 16). Since the major feature of PTR is its superior sensitivity to electronic carrier plasma waves, most (but not all) applications to-date have only involved the con-

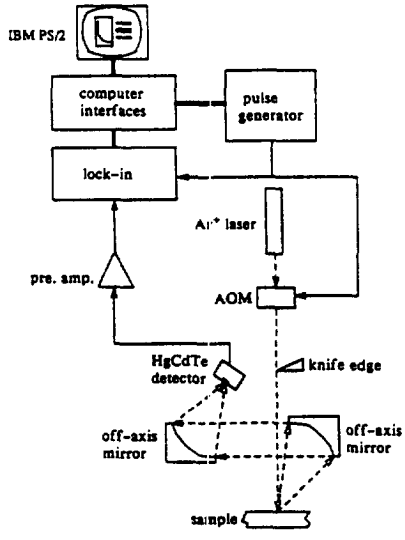

Fig. 4. Typical experimental system for photothermal radiometry of semiconductors

sideration of the term proportional to $\int \Delta N(z;\, \omega)\, dz$ in Equation (16).

4. PTR APPLICATIONS TO SI SUBSTRATE WAFERS AND DEVICES

4.1. *Experimental*

A typical experimental setup for PTR diagnostics of semiconductors is shown in Fig. 4[35]. A harmonically modulated super-bandgap laser beam is obtained by using an acousto-optic modulator (AOM) and is slightly focused on the sample, or unfocused, to the size of approximately 1–5 mm diameter to satisfy the one-dimensionality of the PTR signal model. The resulting infrared blackbody radiation emitted from the semiconductor surface is collimated and collected by two off-axis paraboloidal mirrors and is detected using a liquid nitrogen-cooled photoconductive mercury–cadmium–telluride (MCT) detector. The typical frequency bandwidth of the detector–preamplifier system is dc-1.5 MHz, capable of capturing PTR decay events on the order of 1 MHz, *i.e.*, well within the recombination lifetime range of Si. Faster decays may also be monitored using photovoltaic MCT detectors. The baseline drift of the detector associated with the dc-level is minimized by choosing low-frequency preamplifier cut-off filters in the 0.1 Hz range, which exclude the dc level. The output signal from the MCT/preamplifier is directed to a lock-in amplifier. For deep-level transient spectroscopic radiometry (PTR–DLTS;[35]), the setup has the capability of scanning the sample temperature.

4.2. *Applications to solid-state electronics*

4.2.1. *Quantitative PTR of Si wafers: τ, s, and D measurements.* The modulation frequency range chosen for this important application is between 100 Hz and 100 kHz. The lower limit is chosen so as to prevent the thermal-wave component from dominating the PTR signal. In this frequency range, the thermal-wave component of Equation (16) is neglected, and the plasma-dominated signal is proportional to $\int \Delta N(z, \omega)\, dz$, or, for a sample of thickness L:

$$S_{\mathrm{PTR}}(\omega) = \frac{C_N}{D_n \sigma_n (\beta_v^2 - \sigma_n^2)} \times \left(\frac{\gamma_1 \Gamma_2 - \gamma_2 \Gamma_1 e^{-(\beta_v + \sigma_n)L} + \gamma_1 e^{-\sigma_n L} - \gamma_2 e^{-\beta_v L}}{\Gamma_2 - \Gamma_1 e^{-2\sigma_n L}} - \frac{\sigma_n}{\beta_v}(1 - e^{-\beta_v L}) \right) \quad (20)$$

where β_v is the absorption coefficient at the excitation wavelength. Assuming strong optical absorption at the front surface (optically opaque sample, $\beta_v L \gg 1$, and, in addition, $\beta_v \gg |\sigma_n|$), for a Si wafer with rough unpolished back surface, $s_2 \gg D_n |\sigma_n|$, it follows that the plasma-wave coefficient $\Gamma_2 \approx -1$ in Equation (20), and the PTR signal can be written as

$$S_{\mathrm{PRT}}(\omega) = \frac{C_N}{D_n \sigma_n (D_n \sigma_n + s_1)} \left(\frac{(1 - e^{-\sigma_n L})^2}{1 + \Gamma_1 e^{-2\sigma_n L}} \right) \quad (21)$$

The first reported experimental amplitude PTR frequency-scan data were those by Sheard *et al.*[21]. Those authors estimated carrier lifetimes and surface recombination velocities from their curves, using a semi-infinite PTR model. Salnick *et al.*[28], however, have utilized *both* output signal channels of the lock-in amplifier for fitting the simplified theory, Equation (21), to the PTR signal, with the finite thickness of the wafer taken into account. The lock-in signal output was resolved in in-phase (IP) and quadrature (Q) components. The Q-component was

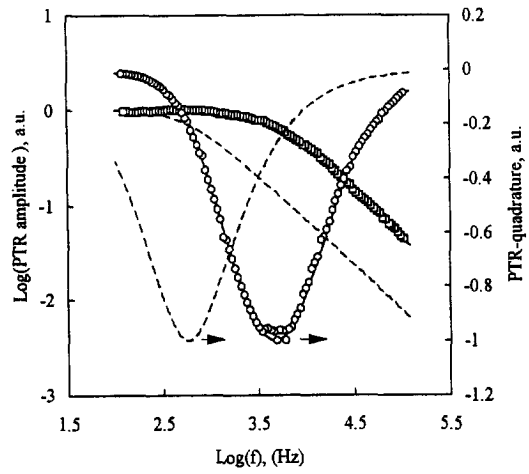

Fig. 5. Experimental PTR amplitude and quadrature component frequency responses of a p-Si sample obtained at 300 K and the results of the best fitting (superposed on the data points) with $D_p = 32\ \mathrm{cm^2/s}$. $s_1 = 210\ \mathrm{cm/s}$ and $\tau = 350\ \mu\mathrm{s}$. The dashed lines represent the frequency responses simulated using the same parameters and the semi-infinite model

found to be an important and useful signal channel in PTR studies of semiconductors. Being close to zero at both low and high frequency limits, it exhibits a sharp clear negative peak at the modulation frequency where $\omega\tau \sim 1$, thus allowing for a faster estimation of the lifetime than the use of the PTR phase. One FZ p-Si wafer (10–15 Ω·cm, $L = 525\ \mu$m) was studied. According to the manufacturer's certificate it had a lifetime $\tau > 100\ \mu$s at room temperature. Figure 5 represents the experimental PTR-amplitude and quadrature responses, which follow the theoretical predictions of Equation (21). The high-frequency log–log amplitude slope of −1 indicates a low surface recombination velocity s_1[36]. The three-parameter fitting of the foregoing frequency responses to the theoretical model, Equation (21), resulted in excellent correlation (solid lines in Fig. 5 are overlapped by the experimental points) and yielded the following carrier transport parameters: $\tau = 350\ \mu$s, $s_1 = 210$ cm/s, and $D_p = 32$ cm^2/s. The importance of accounting for the finite thickness of the Si wafer is clear from the comparison of experimental data and corresponding fitting curves with responses simulated by use of the same parameter values and a semi-infinite model for the PTR signal derived from Equation (21) with $L \to \infty$. These simulations are represented as dashed lines in Fig. 5 and they would erroneously predict a significantly longer lifetime, if the actual wafer thickness were not taken into account.

Another important issue for quantitative PTR is the problem of uniqueness of the measured set of values for the parameters (τ, s_1, D). Assuming the literature value of D, as the least sensitive parameter to processing and/or surface conditioning, one ends up with the issue of uniqueness of the pair (τ, $s_1 \equiv s$). If only the amplitude data are used for a two-parameter fit to the relevant PTR frequency-response Equation (21), as was done by Sheard *et al.*[21], it turns out that the pair of (τ, s) values is cross-compensating to a significant extent: within a certain range of parameter values, changes in the shape of the PTR-amplitude-frequency response introduced by varying s can be compensated by a corresponding adjustment of τ. As a result, there is a number of (τ, s) pairs which would fit a given PTR-amplitude curve. In this light, the estimates given by Sheard *et al.*[21] based on a single signal channel are not absolutely reliable. To overcome this problem, Salnick *et al.*[28] and Salnick and Mandelis[37] fitted the experimental amplitude and quadrature, and amplitude and phase, respectively, to the theory *simultaneously*, thus equating the number of variables with the number of independent sets of data and reducing significantly, or eliminating, the multi-pair solutions to the (τ, s) determination. Figure 6 illustrates the advantage of this approach over the earlier methodology: four (τ, s) pairs with carrier lifetime varying between 0.6 ms and 1.8 ms satisfy the standard deviation constraints imposed on the fit (5% in amplitude-only fitting). On the other hand, only one pair satisfies the simultaneous requirements of amplitude and phase fitting under the same constraint. All other value pairs produce significant deviations from the experimental phase data. It has been shown[37] that the uniqueness problem of the measured parameters becomes more acute in the case of wafers with higher surface recombination velocities than the high-surface-quality wafer used in this example.

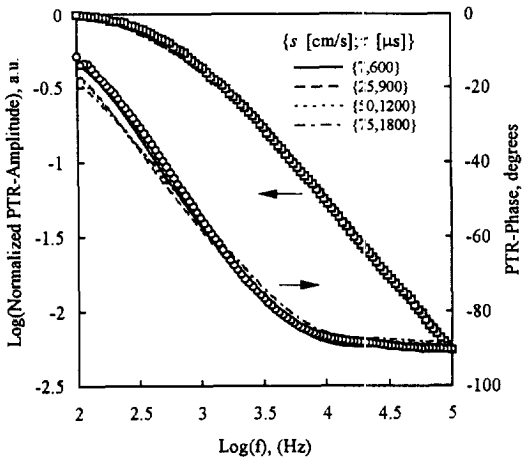

Fig. 6. Experimental PTR amplitude and phase frequency responses obtained from a high-quality FZ Si wafer, and the results of two-parameter fitting to the model of Equation (21) with $L = 500\ \mu$m and $D_n = 12$ cm^2/s. The values of (τ, s) pairs that fit the amplitude curve within the imposed 5% deviation are given in the inset. Only the pair (600 μs, 7 cm/s) satisfies the simultaneous-fit requirement to amplitude *and* phase

4.2.2. *Wafer contamination control by PTR τ measurements.* Equation (21) shows that at low modulation frequencies and for small surface recombination velocities, the PTR signal is real and is given by:

$$S_{PRT} = C_N \frac{\tau}{D_n} \left(\frac{(1 - e^{-L/\sqrt{D_n \tau}})^2}{1 + e^{-2L/\sqrt{D_n \tau}}} \right) \qquad (22)$$

Therefore, the signal phase is zero, and the amplitude becomes directly proportional to the photoinjected carrier lifetime, provided that the wafer thickness is large compared to the dc carrier diffusion length. As frequency increases, a critical value $f = f_c$ is attained, such that the quadrature component deviates from the zero baseline and exhibits a negative peak when $2\pi f_c \tau = 1$, as shown in Fig. 5. This feature allows the quick characterization of process wafers. Six 100 mm diameter FZ p-type Si wafers, 10–15 Ω·cm, with nominal lifetime > 100 μs, and thickness 510–540 μm, each with a different number of gate oxidation treatments, were studied. After each oxidation cycle a specified thickness of oxide was removed, so that all wafers had the same 350 Å of oxide layer. The values of the carrier life-

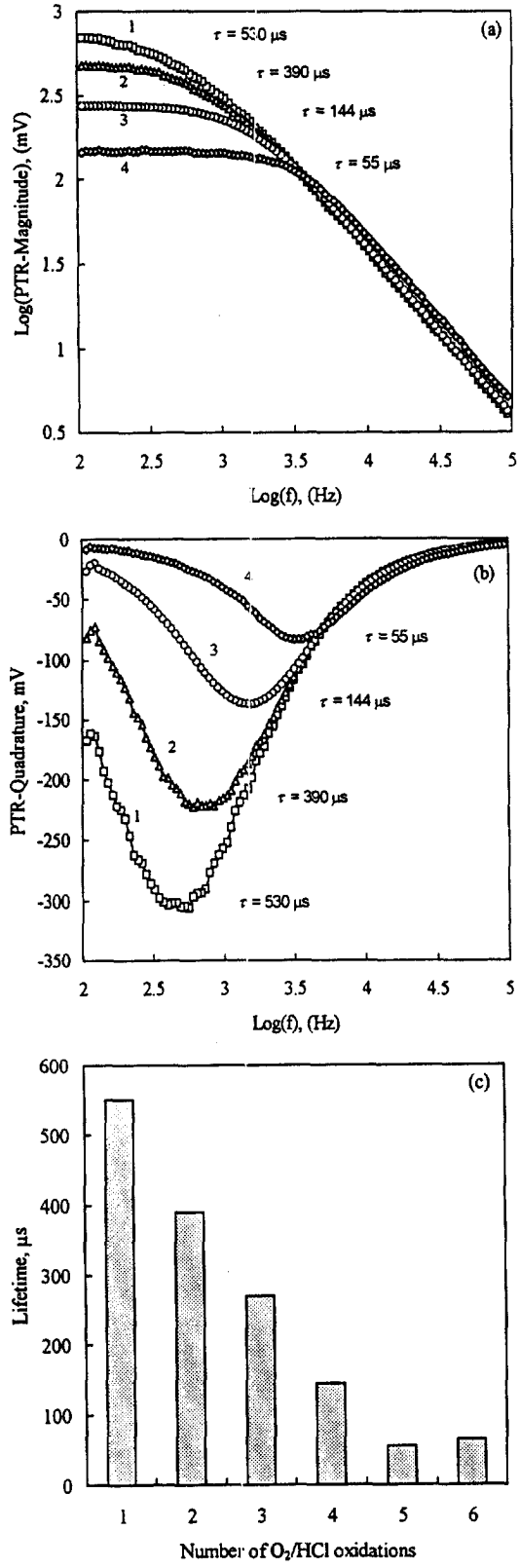

Fig. 7. (a) PTR amplitudes, and (b) PTR quadratures from four FZ p-type Si wafers subjected to one and up to four oxidation cycles as indicated. The measured photoinjected carrier lifetimes are also indicated; (c) Lifetime histogram for all six wafers

times obtained from the fits of the amplitude and quadrature responses, Fig. 7(a), (b), to Equation (21) show the trends indicated by Equation (22) at very low frequencies $f \ll f_c$: the signal magnitude increases proportionally to the measured value of the lifetime; the signal quadrature exhibits a minimum which shifts to lower frequencies with increased lifetime, and tends to return to the zero value for $f \ll f_c$. The histogram on Fig. 7(c) shows the effect of oxidation history on the value of the photoinjected carrier lifetime, in terms of a dramatic decrease of this parameter with the number of oxidation treatments. It is well-known that oxidation is a major source of Si wafer contamination by heavy metals and other impurities and PTR is shown to be a sensitive technique for monitoring furnace contamination.

4.2.3. *PTR of SiO_2/Si MOS capacitor structures.* The modulation frequency range used in these experiments was 100 Hz–120 kHz. Temperature ramps were also introduced by a heater/temperature controller with the entire process controlled by the computer[34]. The heating system was capable of varying and maintaining the sample temperature up to 473 K. Two Si wafers containing multiple MOS capacitor structures were studied. An Al-gated MOS structure (sample W1) had the following parameters: Al layer thickness 0.8 μm, oxide thickness 0.1 μm, n-Si substrate with resistivity ρ = 10–15 Ω·cm and impurity levels of $N \sim 2.5 \times 10^{14}$ cm^{-3}. The gate area was 2.1×10^{-2} cm^2. In sample W2 the gate was n-type poly-Si of 0.35 μm thickness and ρ = 30 Ω·cm. The oxide thickness was 0.08 μm and the substrate was n-Si with ρ = 10–15 Ω·cm and $N \sim 9 \times 10^{14}$ cm^{-3}. PTR signal curves similar to those of Fig. 6 were obtained. Figure 8 shows the PTR lifetime temperature dependence of samples W1 and W2, obtained by fitting the data to Equation (21). Owing to the T-dependence of the prefactor C_N in Equation (19), the amplitude tended to increase with increasing temperature; therefore all experimental curves were normalized to outline only the changes in shape with increasing T. The increase in τ with temperature observed with both wafers follows the Shockley–Read–Hall theory[38,39], which assumes that the thermally increased density of intrinsic carriers fills up existing trapping sites and thus increases the photoinjected carrier lifetime. For the carrier diffusion coefficient, a decreasing dependence on temperature was found for both samples:

$$D(T) = \text{const.} \times T^{-1.5} \qquad (23)$$

This is in reasonable agreement with known[40] and photothermally measured[41] rates. The corresponding Arrhenius plots of the PTR lifetimes and the calculated activation energies are presented in Fig. 9. The activation energy value of ΔE = 0.21 eV obtained for sample W2 is probably due to the near-interface shallow electron trap produced

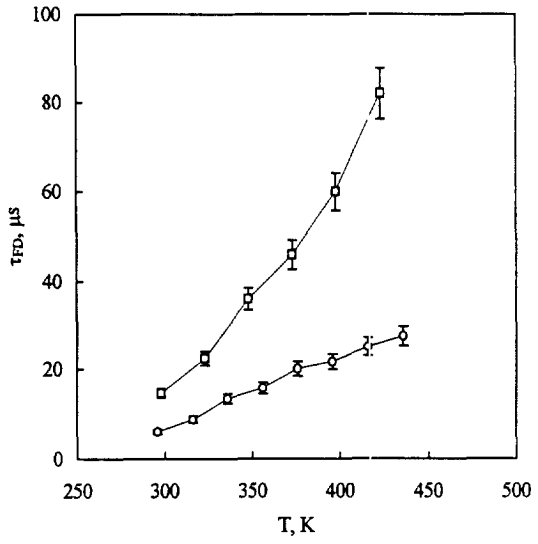

Fig. 8. PTR-measured lifetime temperature dependencies of sample W1 (○) and W2 (□) obtained by simultaneously fitting the amplitude and phase frequency responses

during the gate layer growth. The lifetime information obtained from Fig. 8 shows that the poly-Si gateMOS devices are predicted to exhibit better performance than the metal-gated ones, as expected from the relative unavailability of metallic deep levels in the former capacitors, which are known to act as lifetime killers.

4.2.4. *Depth profilometry of ion-implanted Si wafers.* Recently, a generalized theoretical methodology for carrier lifetime and diffusivity depth profile reconstruction has been developed[42]. This was the result of the realization that an electron–hole photoexcited plasma in semiconductors behaves like a carrier density diffusive wave, and, therefore, it can theoretically be treated as a plasma harmonic oscillator (PHO). The generalized Hamilton–Jacobi plasma-wave theory of a continuously inhomogeneous semiconductor with arbitrary $\tau(x)$ and $D(x)$ depth profiles[42] has been used to reconstruct depth profiles of P^+-implanted, $10^{13}\,cm^{-2}$, 50 keV, and annealed Si samples. The method of simultaneously fitting the amplitude and phase PTR data to the one-dimensional theory of the electronic component of Equation (16)[28] was applied to measure the carrier diffusivity, lifetime and surface recombination velocity of a non-implanted reference sample. The values $\tau = 75\,\mu s$, $D_n = 20\,cm^2/s$ and $s = 800$ cm/s were thus obtained. Figure 10 shows the $M(\omega)$ ratios of the experimental PTR amplitudes obtained for the implanted and annealed Si samples, normalized to that from the reference non-implanted sample. In this manner the experimental frequency data become independent of the transfer function of the instrumentation that produced it. The modulation frequency was between 1 kHz and 1 MHz, in order to exclude the contribution of thermal waves to the total PTR signal. This contribution increases with increased ion implantation damage in Si. As can be seen from Fig. 10, the process of ion implantation introduces a significant change in the PTR-amplitude frequency responses with respect to those of the non-implanted sample. It is seen that the 350°C–1100°C anneals only partially restored the damaged sub-surface layers and reduced the number of electronically sensitive defects in the material bulk to varying degrees, depending on the departure of the $\log(|M(\omega)|$ from the zero (reference) line level in Fig. 10. The most effective restoration of the electronic properties of an implanted sample appears to be the anneal at

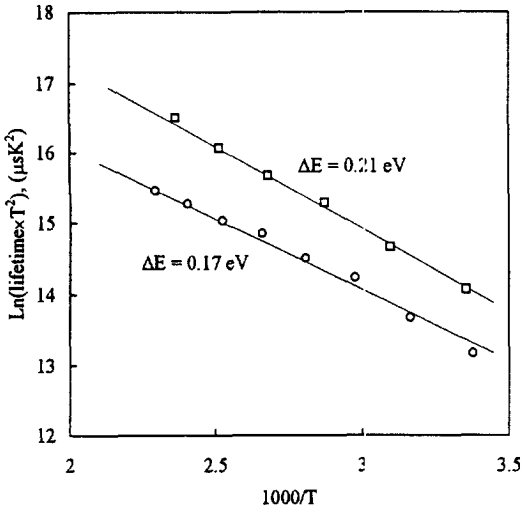

Fig. 9. Arrhenius plots of the PTR-measured lifetimes of samples W1 (○) and W2 (□) and corresponding activation energy levels

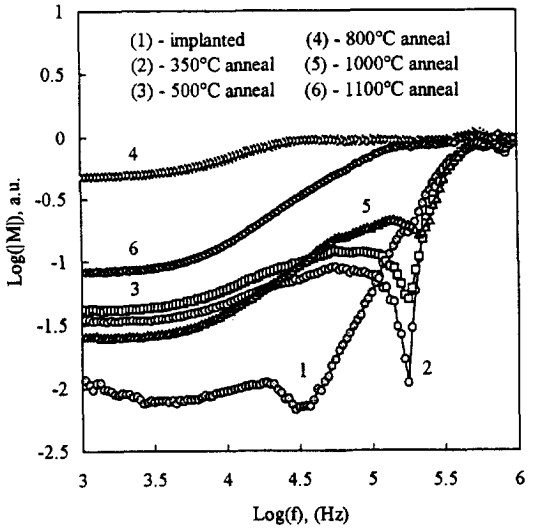

Fig. 10. Experimental PTR-amplitude frequency responses obtained for Si samples implanted with P^+ ions ($10^{13}\,cm^{-2}$, 50 keV) and thermally annealed at different temperatures. The curves are normalized to those obtained for non-implanted Si

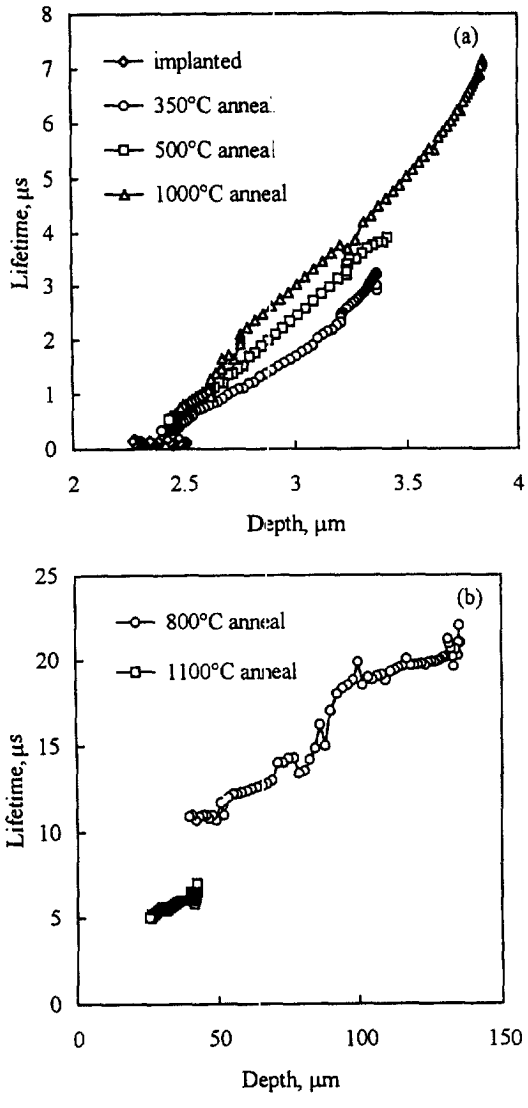

Fig. 11. Results of the reconstruction of the carrier lifetime depth profiles from the experimental frequency responses shown in Fig. 10. Note the difference in depth scales in (a) and (b)

800°C. This is consistent with the effects of negative annealing known from prior modulated thermoreflectance studies of ion-implanted Si[43].

The inversion algorithm which allows for the reconstruction of the $\tau(x)$ profiles[42] is able, in principle, to reconstruct arbitrary carrier lifetime and/or diffusivity depth profiles. Figure 11(a), (b) show the results of carrier lifetime reconstruction from the experimental PTR-amplitude and phase (not shown) normalized frequency responses of Fig. 10. As expected, the ion-implanted unannealed sample with highly damaged sub-surface layers has a very short near-surface (≤ 2 μm) carrier lifetime of about 0.2 μs. Annealing treatments at 350°C and 500°C increased the near-surface τ values up to 3–4 μs, within 3–4 μm of depth (Fig. 11(a)). The most effective lifetime restoration, however, appears to be

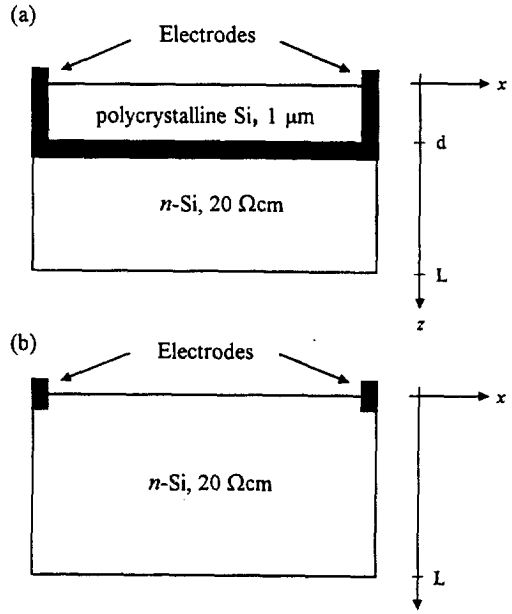

Fig. 12. Cross-sectional views of the photoconductive Si devices: (a) Thin-film photoconductor; (b) Substrate bulk crystalline Si photoconductor

produced after the thermal annealing at 800°C, Fig. 11(b), which resulted in a nearly homogeneous carrier lifetime depth profile, with much longer τ values (10–20 μs) in the bulk. Nevertheless, further increase of the annealing temperature has not improved the electronic property restoration. The thermal treatment at the highest temperature of 1100°C allows improvement of the electronic properties over the 1000°C anneal, and brings the near-bulk carrier lifetime values close to 6 μs, Fig. 11(b), a level only second to the 800°C anneal.

4.2.5. *PTR applications to bulk and thin-film photoconductive devices.* Substrate n-type Si wafers of resistivity $\rho = 20\ \Omega$·cm, were oxidized thermally at 1150°C for 17 h. The oxidation was followed by low-pressure chemical vapor deposition (LPCVD) at 630°C and 500 mTorr of thin polycrystalline Si films 1 μm thick. The thin films were implanted with P^+ ions at 200 keV and fluences up to 10^{15} cm^{-2}, followed by a thermal anneal at 1000°C for 1 h, in order to electrically activate the implanted impurities and stabilize the grain size. Inspection with electron microscopy revealed a grain size of ≈500 Å. Subsequently, conducting electrodes were formed and several dice were cut and placed on ceramic chips. The cross-section of the resulting photoconducting devices is shown in Fig. 12. In this investigation attention was focused on the highest doping-density photoconductors (1×10^{15} cm^{-2}), as they exhibited the strongest free-carrier plasma responses[31].

In addition to the PTR signal, the photocurrent (PC) signal of some devices was also monitored using the ac voltage drop across a small resistor of

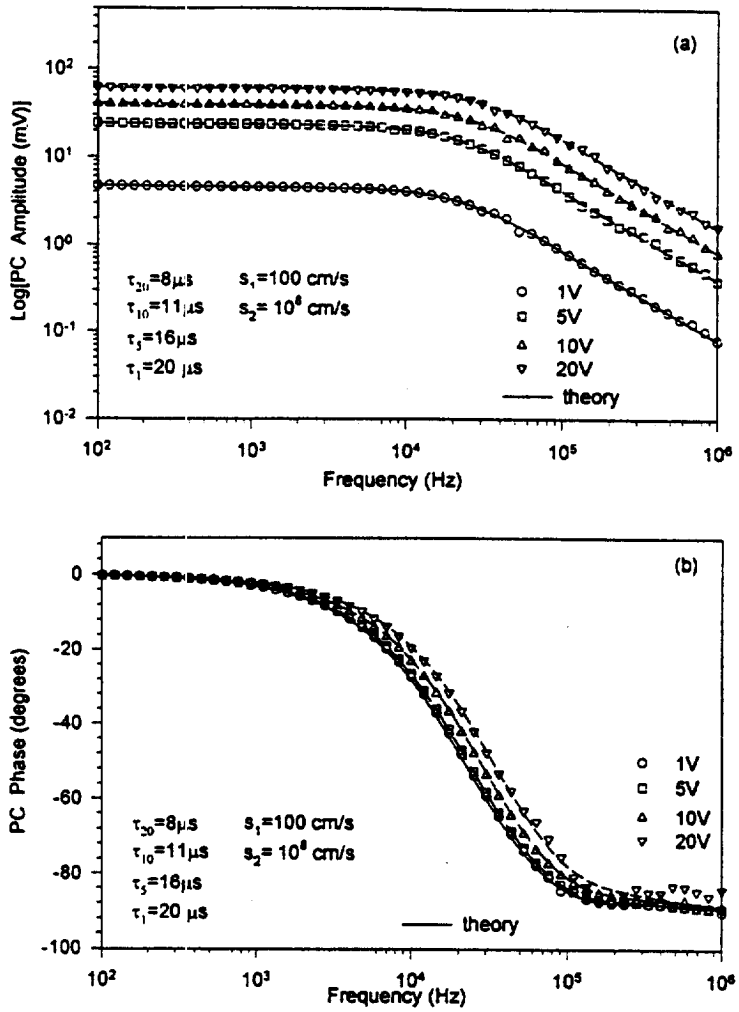

Fig. 13. Amplitude (a) and phase (b) of the PC frequency scans of the substrate-Si photoconductor. Parameters of simultaneous best fits: $D = 20\ \text{cm}^2/\text{s}$; $L = 250\ \mu\text{m}$; $s_1 = 10^2\ \text{cm/s}$; $s_2 = 10^8\ \text{cm/s}$. τ_j indicates the best-fit lifetime at applied dc voltage (j)

known resistance value, carrying the photocurrent generated by the modulated laser beam photocarrier injection, and oriented by a transverse dc field applied across the electrodes of the sample. In this case the presence of an applied bias generated a strong thermal-wave field due to the Joule-effect heating, in addition to the source components given by Equations (1) and (2):

$$H(z,\omega) = \frac{\eta_{NR}(h\nu - E_G)}{h\nu}\beta_v I_0 e^{-\beta_v z} + \frac{\eta_G \eta_{NR} E_G}{\tau}\Delta N(z,\omega) + E \cdot J(z,\omega) \quad (24)$$

Here **E** is the applied transverse electric field between the electrodes (x-direction in Fig. 12) and **J** is the transverse current density. To determine the term **E**·**J** use can be made of the experimental fact that the photocurrent data from the bulk samples were consistent with a contribution from only the drift component. Therefore, the diffusion current density along the x-direction of Fig. 12 was neglected:

$$E \cdot J(z,\omega) = q\mu E^2 \Delta N(z,\omega) \quad (25)$$

In the bulk photoconductor, the total current density consisted of all the individual depth contributions to the collecting electrodes:

$$J_n(\omega) = q\mu_n E \int_0^L \Delta N(z,\omega)\,dz \quad (26)$$

Fig. 13 shows the results of PC frequency scans with the bulk-Si photoconductor and theoretical fits of Equation (26), using the photoinjected carrier distribution of Equation (9). Figure 14 shows the PTR frequency scans of the same sample. Both amplitude and phase have been fitted to Equation (16), with the subsidiary Equation (9) for

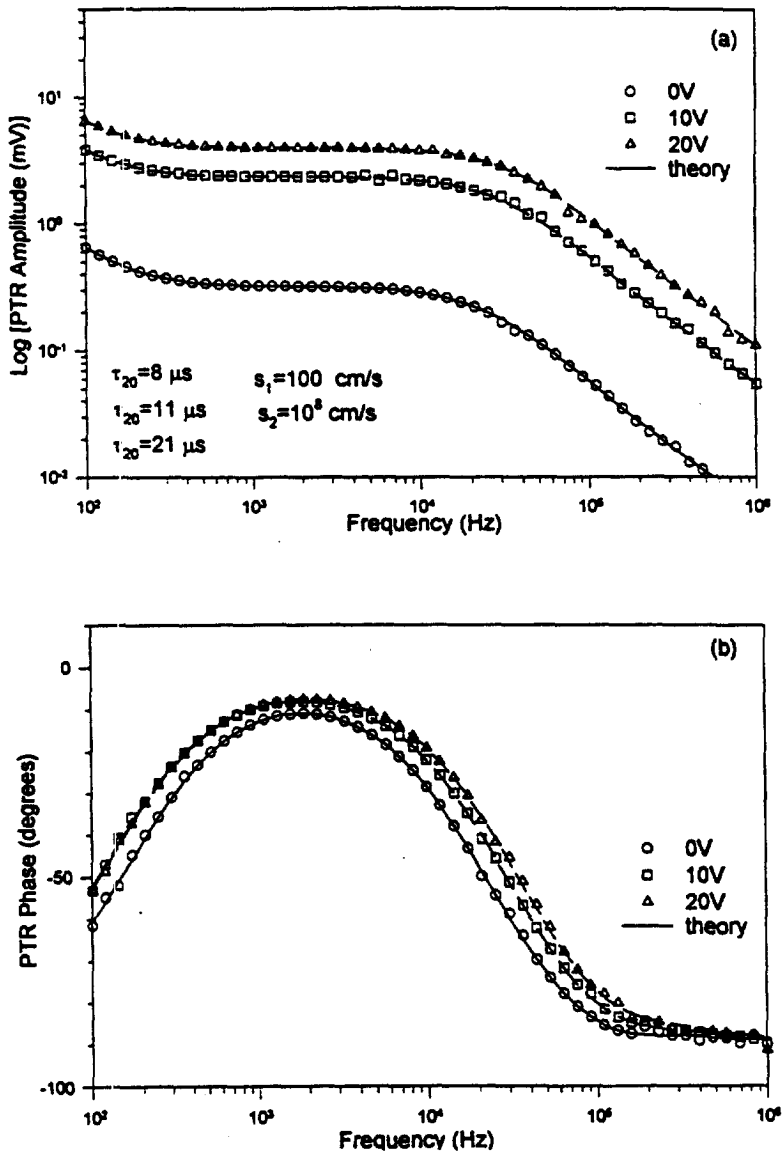

Fig. 14. Amplitude (a) and phase (b) of the PTR signal frequency scan of the device of Fig. 12(b) and Fig. 13. D, τ, s_1, and s_2 values are as in Fig. 13. Best-fitted α value: 1.0 cm^2/s. Best fitted C_N value in Equation (16), for all three curves: 1×10^{-16} Wm^2; best-fitted C_T values: 3.8×10^6 W/mK (V = 0 V); 2×10^5 W/mK (V = 10 V); and 5.5×10^4 W/mK (V = 20 V)

the thickness-integrated free-carrier density wave, and the following expression for the thickness-integrated thermal wave[31]

$$\int_0^L \Delta\Theta(z,\omega)\,dz = \frac{1}{\sigma_t}[(1-e^{-\sigma_t L})F_1 + F_2] - \left(\frac{C_0 N_0}{\sigma_e}\right) \times (1-e^{-\sigma_e L})(\Gamma_2 + e^{-\sigma_e L}) \quad (27)$$

where, for either type of carrier, σ_e is given by Equation (12); $\sigma_t = \sqrt{i\omega/\alpha}$ is the complex thermal diffusion coefficient at frequency $f = \omega/2\pi$ (α is the thermal diffusivity of the semiconductor); and the following definitions were also made

$$F_1 = \frac{C_1 + C_2 e^{-\sigma_t L}}{1 - e^{-2\sigma_t L}}; \quad F_2 = \frac{C_1 e^{-\sigma_t L} + C_2}{1 + e^{-\sigma_t L}} \quad (27a)$$

with

$$N_0 = \frac{I_0}{h\nu(D\sigma_e + s_1)(\Gamma_2 - \Gamma_1 e^{-2\sigma_e L})} \quad (27b)$$

and

$$C_0 = \frac{E_g + q\mu_n \tau E^2}{k_b \tau(\sigma_e^2 - \sigma_t^2)} \quad (27c)$$

where k is the thermal conductivity of the semiconductor. Also the parameters C_1 and C_2 were defined as:

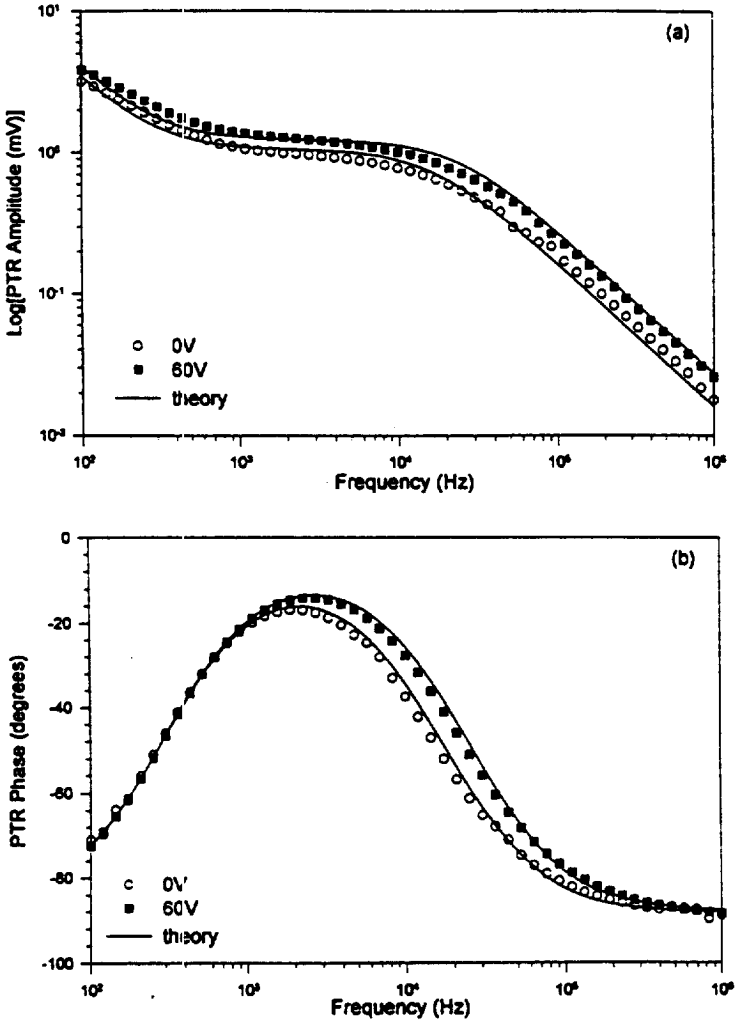

Fig. 15. Amplitude (a) and phase (b) of the PTR signal frequency scan of the thin-film photoconductor of Fig. 12(a). All substrate parameters were assigned the values found for the bulk crystalline Si photoconductor at zero bias. Thin-film values: $D_f = 9\ \mathrm{cm^2/s}$; $d = 1\ \mu\mathrm{m}$; $\alpha_f = 0.1\ \mathrm{cm^2/s}$; $k_f = 15\ \mathrm{W/mK}$; $s = 104\ \mathrm{m/s}$; $\tau_f = 11\ \mu\mathrm{s}$ ($V = 0$ V), and $6\ \mu\mathrm{s}$ ($V = 60$ V)

$$C_1 = \frac{I_0(h\nu - E_g)}{h\nu k\sigma_t} + \frac{N_0}{\sigma_t k}[s_1 E_g(\Gamma_2 + e^{-2\sigma_e L}) + \sigma_e k C_0(\Gamma_2 - e^{-2\sigma_e L})] \quad (27d)$$

and

$$C_2 = \frac{N_0 e^{-\sigma_e L}}{\sigma_t}\left[\frac{s_2 E_G(\Gamma_2 + 1)}{k} + \sigma_e C_0(1 - \Gamma_2)\right] \quad (27e)$$

In each of the various dc-voltage-dependent curves of Fig. 14, the prefactors C_N and C_T in Equations (17) and (19) were adjusted accordingly, so as to produce additively the optimal overlap in thermal- and electronic-wave components. This was rather straightforward, as the thermal wave affects primarily the low-frequency end (< 1 kHz), whereas the plasma-wave dominates the high frequency end. The best fits to the data of Fig. 14 gave the lifetime-electronic diffusivity pairs measured from the PC data of Fig. 13, a fact which indicates identical electronic PTR and PC signal production mechanisms. The low-frequency data were sensitive to the actual value of the thermal diffusivity of Si, which was found to be $1.0\ \mathrm{cm^2/s}$, in excellent agreement with literature values[44]. Upon plotting the PTR amplitude *vs.* the square of the applied dc bias, V_{dc}^2 a straight line relationship was found throughout the entire range of dc biases (0–30 V). This result validates the theory of electronic drift mechanism, in agreement with Equations (24)–(27). As shown in Figs 13 and 14, the lifetime values exhibited a decrease with increasing dc bias. The foregoing facts suggest that the dc temperature increase of the bulk photoconductor sample due to Joule heating affects the photoinjection lifetime values in a manner consistent with the Shockley–Reed–Hall recombination mechanism. The best-fitted τ and D values are well within the accepted norms of recombination lifetimes in Si[45].

The PTR response to the thin-film device of Fig. 12(a) is shown in Fig. 15. In this case, substantial increase of the applied bias resulted only in small changes in the PTR signals, owing to the much higher resistivity exhibited by these thin films compared to the crystalline Si photoconductors. Knowledge of the substrate lifetime τ was an important input, as this is a parameter to which the fitting to a modification of Equation (16) was sensitive

$$\int_0^L \Delta N_T(z, \omega)\, dz = \langle \Delta N(\omega) \rangle d + \int_0^L \Delta N(z, \omega)\, dz \tag{28}$$

Here d is the thin-film thickness, Fig. 12(a), $d \ll L$, ΔN_T is the total photoexcited carrier density (both thin-film and substrate), $\Delta N(z,\omega)$ is given by Equation (9), and the depth-averaged thin-film quantity on the right hand side is dependent on the thin-layer plasma-wave complex coefficient $\sigma_{nf}(\omega)$[31], which is defined completely analogous to that of a bulk sample, Equation (12). This allowed the unique fixing of the surface thin-film photoconductor layer lifetime, τ_f, as shown in the caption of Fig. 15, a very important parameter for the operation of the photoconductive device and quite difficult to obtain otherwise.

5. CONCLUSIONS

Laser infrared photothermal radiometry (PTR) of semiconductors is a novel sensitive, non-contact, all-optical carrier diffusion-wave diagnostic technique based on the physics of optical injection and infrared blackbody emission from de-exciting carriers in a solid-state electronic material. Its physical principles, experimental set-up, and the first applications have been presented in this article. It was shown that PTR is capable of yielding accurate measurements of carrier transport parameters, principally the photoinjected carrier lifetime, the diffusion coefficient and the surface recombination velocity, by the *simultaneous* measurement and theoretical analysis of both lock-in-amplifier demodulated amplitude and phase (or in-phase and quadrature) data. The technique of frequency-scanned PTR is very efficient in decoupling *easily and totally* the thermal from the plasma evolution effects, a task which is, at best, quite cumbersome with other combinations of photothermal measurement methodologies[25]. The theoretical development was followed by the description of the first few applications to Si-based materials and devices: electronic transport properties of substrate wafers; MOS capacitor structure lifetimes and their dependence on sample temperature, with the ability to extract the activation energy of the lifetime-limiting mechanism (a novel PTR–DLTS technique); the first-ever lifetime depth profiles of ion-implanted wafers through the consideration of the carrier plasma-wave inverse problem; and bulk-Si crystalline and thin-film device characterization with respect to photoinjected carrier lifetime and electronic diffusivity. At low frequencies the signal domination by thermal-wave effects allows the measurement of the thermal diffusivity of the electronic material, as well.

Based on the rapidly expanding PTR applications to solid-state electronics, there are excellent prospects for the novel technique to be developed to a remote, fully non-contacting, process quality control diagnostic for semiconductor manufacturing, specifically for (i) real-time *in-situ* characterization of transport properties of substrates and thin-film devices; (ii) wafer native and process-induced deep-level defects via PTR–DLTS; and (iii) for fast, high-spatial-resolution scanning imaging and mapping of lifetimes over the wafer surface. Work is continuing in the author's laboratory toward a full comparison of PTR lifetime and diffusion coefficient measurements (and thus of carrier diffusion lengths) with conventional industrial wafer monitoring technologies, such as surface photovoltage (SPV) and electrical/optical DLTS.[46]

Acknowledgements—The author would like to acknowledge the support of the Natural Sciences and Engineering Research Council of Canada through several Research Grants, which transformed the development of laser-induced PTR into a novel, promising diagnostic technique, suitable for applications to solid-state electronics.

REFERENCES

1. Hess P., (Ed.), *Photoacoustic, Photothermal and Photochemical Processes at Surfaces and in Thin Films*, Springer-Verlag, Berlin, 1989.
2. A. Mandelis (Ed.), *Progress in Photothermal and Photoacoustic Science and Technology*, Vol. I, Elsevier, New York, 1992.
3. Bialkowski, S. E., *Photothermal Spectroscopy Methods for Analysis*, Chemical Analysis, Vol. 134, Wiley, New York, 1996.
4. van Driel, H. M., *Physics of Pulsed Laser Processing of Semiconductors in Semiconductors Probed by Ultrafast Laser Spectroscopy* (Edited by R. R. Alfano), Vol II, p.61. Academic Press, Orlando, FL, 1984.
5. Bandeira, I. N., Closs, H. and Ghizoni, C. C., *J. Photoacoust.*, 1982, **1**, 275.
6. Quimby, R. S. and Yen, W. M., *J. Appl. Phys.*, 1980, **51**, 4985.
7. Thielemann, W. and Rheinländer, B., *Solid-State Electron.*, 1985, **28**, 1111.
8. Flaisher, H. and Cahen, D., *IEEE Trans. UFFC*, 1986, **13**, 622.
9. Nordal, P.-E. and Kanstad, S. O., *Appl. Phys. Lett.*, 1981, **38**, 486.
10. Imhof, R. E., Zhang B. and Birch, D. J. S., in Non-Destructive Evaluation (Edited by A. Mandelis), *Progress in Photothermal and Photoacoustic Science and Technology*, Vol. II, Prentice-Hall, Englewood Cliffs, NJ, Chap. 7, 1994.
11. Prahl, S., in Life and Earth Sciences (Edited by A. Mandelis and P. Hess), *Progress in Photothermal and*

Photoacoustic Science and Technology, Vol. III, SPIE Opt. Eng. Press, Chap. 11, 1997.
12. Welch, A. J. and van Gemert M. J., (Eds.), *Optical-Thermal Response of Laser-Irradiated Tissue*, Plenum, New York, 1995.
13. Nakamura, H., Tsubouchi, K., Mikoshiba, N. and Fukuda, T., *Jpn. J. Appl. Phys.*, 1985, **24,** L876.
14. Mikoshiba, N. and Tsubouchi, K., in *Photoacoustic and Thermal Wave Phenomena in Semiconductors* (Edited by A. Mandelis), North-Holland, New York, Chap. 3, 1987.
15. Sheard, S. J., Photothermal Radiometric Microscopy, Ph.D. Thesis, Univ. College London, 1987.
16. Spitzer, W. G. and Fan, H. Y., *Phys. Rev.*, 1957, **106,** 882.
17. Spitzer, W. G. and Whelan, J. M.. *Phys. Rev.*, 1959, **114,** 59.
18. Kachare, A. H., Spitzer, W. G., Euler, F. K. and Kahan, A., *J. Appl. Phys.*, 1974, **45**, 2938.
19. Sopori, B. L., *Appl. Phys. Lett.*, 1985, **47,** 39.
20. Ulmer, E. A. and Frankl, D. R. *Proc. IXth Int. Conf. Physics Semiconductors*, Nauka, p. 170, 1968.
21. Sheard, S. J., Somekh, M. G. and Hiller, T., *Mater. Sci. Eng. B*, 1990, **5,** 101.
22. Little, I., Crean, G. M. and Sheard, S. J., *Mater. Sci. Eng. B*, 1990, **5,** 89.
23. Baltes, H. P. in *Progress in Optics* (Edited by E. Wolf), North-Holland, Amsterdam, Chap. I, 1976.
24. Cho, K. and Davis, C. C., *IEEE J. Quant. Electron.*, 1989, **25,** 1112.
25. Mandelis, A., (Ed.), *Photoacoustic and Thermal-Wave Phenomena in Semiconductors*, North-Holland, New York, 1987.
26. Salnick, A., Mandelis, A., Ruda H. and Jean, C., *J. Appl. Phys.* 1997, **82**, 1853.
27. McKelvey, J. P., *Solid State and Semiconductor Physics*, Krieger, Malabar, FL, Chap. 10, 1966.
28. Salnick, A., Mandelis, A. and Jean, C., *Appl. Phys. Lett.*, 1996, **69,** 2522.
29. Moss, T. S., Burrell, G. J. and Ellis, B., *Semiconductor Opto-Electronics*, Butterworth, U.K., Chaps. 1–2, 1973.
30. Mandelis, A., Bleiss, R. and Shimura, F., *J. Appl. Phys.*, 1993, **74,** 3431.
31. Mandelis, A., Othonos, A., Christofides, C. and Boussey-Said, J., *J. Appl. Phys.*, 1996, **80,** 5332.
32. Ramo, S., Whinnery J. R. and Van Duzer, T., *Fields and Waves in Communication Electronics*, Wiley, New York, p. 334, 1965.
33. Smith, R. A., *Semiconductors*, 2nd Ed., Cambridge Univ. Press, Cambridge, p. 118, 1978.
34. Salnick, A., Jean, C. and Mandelis, A., *Solid-State Electron.*, 1997, **41,** 591.
35. Chen, Z. H., Bleiss, R., Mandelis, A., Buczkowski, A. and Shimura, F., *J. Appl. Phys.*, 1993, **73,** 5043.
36. Othonos, A., Christofides, C. and Mandelis, A., *Appl. Phys. Lett.*, 1996, **69,** 821.
37. Salnick, A. and Mandelis A. 1997, unpublished.
38. Shockley, W. and Read, W.T., *Phys. Rev.*, 1952, **87,** 835.
39. Hall, R.N., *Phys. Rev.*, 1952, **87,** 387.
40. Boyd, I. W., Binnie, T. D., Wilson, J. I. B. and Coles, M. J., *J. Appl. Phys.*, 1984, **55,** 3061.
41. Lapshin, K. V., Petrovsky, A. N. and Salnick, A., *Tech. Phys. Lett.*, 1993, **19,** 9.
42. Salnick, A. and Mandelis, A., *J. Appl. Phys.*, 1996, **80,** 5278.
43. Vitkin, A., Christofides, C. and Mandelis, A., *Appl. Phys. Lett.*, 1989, **54,** 2392.
44. Touloukian, Y. S., Powell, R. W., Ho, C. Y. and Nicolaou, M. C., *Thermophysical Properties of Matter*, Vol. X, IFI/Plenum, New York, 1973.
45. Jellison, G. E. and Burke, H. H., *J. Appl. Phys.*, 1986, **60,** 841.
46. Edwards, D. F. and Maker, P. D., *J. Appl. Phys.*, 1962, **33**, 2466.